Quasibound states in a chaotic molecular system

Alex M. Barr, Kyungsun Na, and L. E. Reichl[*]

Center for Complex Quantum Systems and Department of Physics, The University of Texas at Austin, Austin, Texas 78712, USA
(Received 1 February 2011; published 20 June 2011)

We show the influence of stable and unstable periodic orbits on the energy eigenstates of the HOCl molecule, both below and above dissociation. The energy range considered is low enough to hold the HO bond fixed, allowing a two-dimensional model of the molecule. Above dissociation unstable periodic orbits, in a chaotic sea, anchor quasibound states of the molecule. Quasibound states are calculated using reaction matrix theory and are found to have lifetimes ranging over five orders of magnitude.

I. INTRODUCTION

Quasibound states are of great importance in molecular systems because of their influence on scattering processes and dissociation rates. Recent studies of the molecule HOCl, in the electronic ground state, reveal quasibound states at energies above the HO + Cl dissociation energy that have lifetimes ranging over several orders of magnitude [1–4]. These studies are all based on the use of absorbing potentials to locate quasibound states. Also, for the most part, the studies focus on quasibound states for cases where the molecule had significant excitation in the HO bond. In the present work, we focus on energies just above dissociation, where the dynamics is largely governed by the motion of HO and Cl, with the very stiff HO bond in its ground state. In this regime, the dynamics of the molecule can be studied using a two-dimensional (2D) model of HOCl in which the HO bond length is held fixed [5,6]. We use a reaction matrix to construct the scattering matrix (*S* matrix) for the Cl-OH scattering process and determine the quasibound states from poles of the *S* matrix. This approach does not require the use of an absorbing potential and allows us to compute scattering states without distortions introduced by absorbing potentials. One of our goals is to show that quasibound states are supported by unstable periodic orbits (POs) in the chaotic sea that governs the dynamics above dissociation.

The analysis of stable POs, and bifurcations in these orbits, in the classical dynamics of HOCl has proven very useful in understanding the energy eigenstates of HOCl below dissociation [3,6,7]. However, no attempt has so far been made to connect the quasibound states in HOCl to the underlying classical dynamics. Recent studies of electron waveguides and laser-driven atomic systems suggest that both stable and unstable POs as well as homoclinic and heteroclinic tangles in the classical phase space can influence the quasibound states of a system [8,9]. The purpose of the current paper is to examine the structure and lifetime of quasibound states using a 2D model of HOCl and to illustrate how these states are influenced by the classical dynamics of the system.

In subsequent sections, we compute both the bound states and the quasibound states of the HOCl molecule. In Sec. II, we derive the Hamiltonian that we use to obtain both types

of states. In Sec. III, we describe the numerical methods we use to construct the Hamiltonian matrix. In Sec. IV, we obtain the bound states and show how they are influenced by the classical stable and unstable POs. In Sec. V, we discuss reaction matrix theory, in the context of the HOCl molecule, and show how we obtain the scattering matrix. In Sec. VI, we describe the quasibound states of the molecule and relate them to the classical dynamics. In Sec. VII, we obtain the Wigner-Smith delay time and in Sec. VIII we make some concluding remarks.

II. TWO-DIMENSIONAL HAMILTONIAN

We consider a 2D model of HOCl in which the HO bond length is held fixed. The classical Hamiltonian for this model is discussed in [5]. We outline here the derivation of the quantum mechanical Hamiltonian operator. Let $\mathbf{t_1}$ be a vector from the center of mass of the HO dimer to Cl and $\mathbf{t_2}$ a vector from H to O (see Fig. 1). With these definitions the kinetic energy operator can be written as

$$\hat{K} = -\frac{\hbar^2}{2M}\nabla^2_{R_{\mathrm{CM}}} - \frac{\hbar^2}{2\mu_1}\nabla^2_{t_1} - \frac{\hbar^2}{2\mu_2}\nabla^2_{t_2}, \qquad (1)$$

where $M = m_{\mathrm{H}} + m_{\mathrm{O}} + m_{\mathrm{Cl}}$, $\mu_1 = \frac{m_{\mathrm{Cl}}(m_{\mathrm{H}}+m_{\mathrm{O}})}{M}$, $\mu_2 = \frac{m_{\mathrm{H}}m_{\mathrm{O}}}{m_{\mathrm{H}}+m_{\mathrm{O}}}$, and R_{CM} is the displacement of the HOCl center of mass in the laboratory frame.

We assume, without loss of generality, that the center-of-mass motion is at rest and introduce Jacobi coordinates: R, the length of $\mathbf{t_1}$; r_0, the length of $\mathbf{t_2}$; and θ, the angle between $\mathbf{t_1}$ and $\mathbf{t_2}$. We denote the body frame (lab frame) coordinates (x,y,z) $[(x',y',z')]$. We assume that the total angular momentum vector lies along the body $\hat{\mathbf{y}}$ axis and that the body $\hat{\mathbf{y}}$ and the laboratory $\hat{\mathbf{y}}'$ axes coincide. We also assume that the motion of HO and Cl is confined to the (x,z) plane and that $\mathbf{t_1}$ always lies along the $\hat{\mathbf{z}}$ axis, making an angle β with the $\hat{\mathbf{z}}'$ axis in the laboratory frame as shown in Fig. 1. The Jacobi coordinates and the angle β can then be written in terms of $\mathbf{t_1}$ and $\mathbf{t_2}$ as follows:

$$R = \sqrt{t_{1x}^2 + t_{1z}^2}, \quad r_0 = \sqrt{t_{2x}^2 + t_{2z}^2},$$

$$\theta = \cos^{-1}\left[\frac{t_{2z}}{\sqrt{t_{2x}^2 + t_{2z}^2}}\right] - \beta, \quad \beta = \cos^{-1}\left[\frac{t_{1z}}{\sqrt{t_{1x}^2 + t_{1z}^2}}\right]. \qquad (2)$$
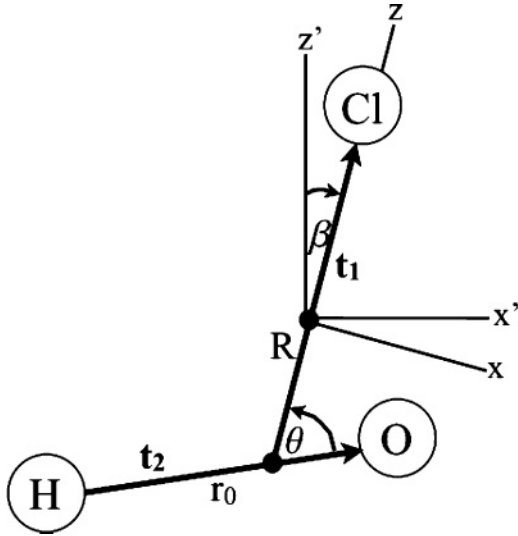
---

[*]reichl@mail.utexas.edu

FIG. 1. Jacobi coordinates R, r_0, and θ. The body-fixed (x,z) and laboratory (x',z') axes differ by an angle β.

Using these relationships and the fact that r_0 is held constant, the kinetic energy operator can be rewritten as

$$\hat{K} = -\frac{\hbar^2}{2}\left[\frac{1}{\mu_1}\left(\frac{\partial^2}{\partial R^2} + \frac{1}{R}\frac{\partial}{\partial R}\right) - \frac{2}{\mu_1 R^2}\frac{\partial}{\partial\theta}\frac{\partial}{\partial\beta}\right.$$
$$\left. + \frac{1}{\mu_1 R^2}\frac{\partial^2}{\partial\beta^2} + \left(\frac{1}{\mu_1 R^2} + \frac{1}{\mu_2 r_0^2}\right)\frac{\partial^2}{\partial\theta^2}\right]. \quad (3)$$

Following the same procedure as above the total angular momentum can be written as $\mathbf{L}_{\text{tot}} = i\hbar\frac{\partial}{\partial\beta}\hat{\mathbf{y}}$. We now further restrict our analysis to motion in which the total angular momentum is 0. This requires that the wave function be independent of β and the 2D Hamiltonian operator for HOCl becomes

$$\hat{H} = -\frac{\hbar^2}{2}\left[\frac{1}{\mu_1}\left(\frac{\partial^2}{\partial R^2} + \frac{1}{R}\frac{\partial}{\partial R}\right) + \left(\frac{1}{\mu_1 R^2} + \frac{1}{\mu_2 r_0^2}\right)\frac{\partial^2}{\partial\theta^2}\right]$$
$$+ V(R,\theta), \quad (4)$$

where $V(R,\theta)$ is the potential energy of interaction between the atoms. The potential energy is derived from the 3D potential energy studied in [3] by setting r_0 equal to its equilibrium value of 1.85 a_0, where $a_0 = 0.52917 \times 10^{-10}$ m is the Bohr radius. A contour plot of the potential energy is shown in Fig. 2(a). The exact expression for the potential energy is given in [5]. Taking the minimum of the potential energy to be $V(R_{\text{eq}},\theta_{\text{eq}}) = 0$, the classical dissociation energy $V(\infty,\theta) = 20,312.3$ cm^{-1}. All energies in the remainder of the paper are given relative to the potential energy minimum.

III. NUMERICAL METHODS

The energy eigenstates of the 2D HOCl molecule are obtained by using a discrete variable representation (DVR) of the Hamiltonian matrix. This method uses a spatially localized basis set in which the potential energy matrix is diagonal. We start by defining a 1D primitive basis in R consisting of 320 sine
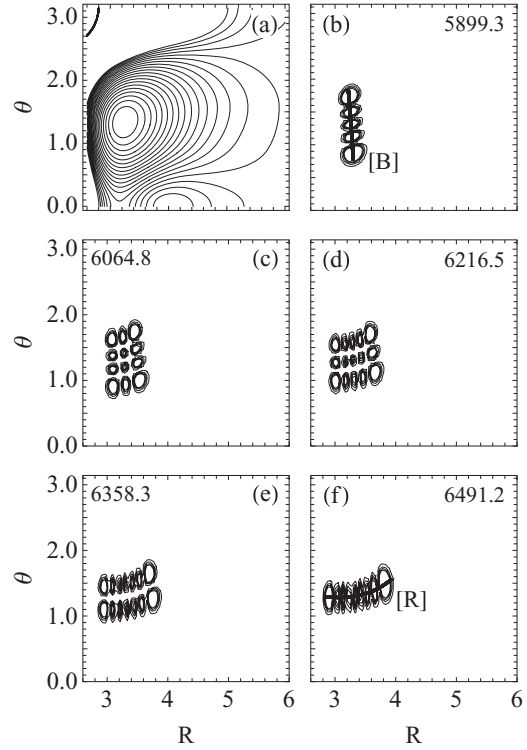

FIG. 2. (a) Contour plot of the 2D potential energy function. (b–f) Energy eigenstates (below dissociation) belonging to polyad $P = 8$, with energies given in cm^{-1}. Eigenstates in (b) and (f) are shown with their corresponding periodic orbits [B] and [R], respectively. Coordinate R is measured in units of a_0.

functions, $\phi_{R,n}(R) = \sqrt{\frac{2}{R\Delta R}}\sin\left[\frac{n(R-R_{\min})\pi}{\Delta R}\right]$, where $\Delta R = R_{\max} - R_{\min}$ with $R_{\max} = 10a_0$ and $R_{\min} = 2a_0$. This primitive basis is used to solve the 1D eigenproblem $[-\frac{\hbar^2}{2\mu_1}(\frac{\partial^2}{\partial R^2} + \frac{1}{R}\frac{\partial}{\partial R}) + V(R,\theta_{\text{eq}})]\psi_{R,n}(R) = E_{R,n}\psi_{R,n}(R)$. The coordinate matrix $\mathbf{R}$ with matrix elements $\mathbf{R}_{m,n} = \int_{R_{\min}}^{R_{\max}}\psi_{R,m}R\psi_{R,n}R\,dR$ is then diagonalized in the eigenbasis $\psi_{R,n}(R)$, where $n = 1...130$. The eigenvectors of $\mathbf{R}$ form a unitary matrix $\mathbf{T_R}$ which transforms the eigenbasis $\psi_{R,n}(R)$ to a DVR basis $\tilde{\psi}_{R,n}(R)$ [10]. The DVR basis function $\tilde{\psi}_{R,n}(R)$ is localized around R_n, the nth eigenvalue of $\mathbf{R}$. Using the 1D eigenstates to build the DVR basis produces a DVR basis that is optimized for our potential energy function.

The potential energy is symmetric about $\theta = 0$, allowing us to treat even and odd parity states separately. For odd states we use a primitive basis of 60 sine functions, $\phi_{\theta,n}(\theta) = \sqrt{\frac{2}{\pi}}\sin(n\theta)$. For even states we use 61 cosine functions, $\phi_{\theta,n}(\theta) = \sqrt{\frac{1}{\pi}}$ if $n = 0$ and $\sqrt{\frac{2}{\pi}}\cos(n\theta)$ otherwise. While there is no coordinate operator for θ as there is for R, we can still define a matrix with elements $\boldsymbol{\theta}_{m,n} = \int_0^\pi \phi_{\theta,m}\theta\phi_{\theta,n}d\theta$ to determine our DVR basis. The $\boldsymbol{\theta}$ matrix is diagonalized to obtain a unitary matrix $\mathbf{T_\theta}$ that transforms between the primitive basis $\phi_{\theta,n}(\theta)$ and the DVR basis $\tilde{\phi}_{\theta,n}(\theta)$ which is localized around the eigenvalues of $\boldsymbol{\theta}$ that span $0 \leqslant \theta \leqslant \pi$. The Hamiltonian is symmetric about $\theta = 0$, which allows us to confine our attention to the upper half-plane in θ when seeking energy eigenstates. The DVR basis we obtain

from our primitive basis in θ yields more highly converged eigenvalues for the 2D Hamiltonian than when we use a "potential-optimized" DVR basis in θ.

The full 2D HOCl Hamiltonian is evaluated in three stages. First, the kinetic energy matrix is built in a direct product basis of $\psi_{R,n}(R)$ and $\phi_{\theta,n}(\theta)$. The potential energy matrix is then built in a direct product DVR basis of $\tilde{\psi}_{R,n}(R)$ and $\tilde{\phi}_{\theta,n}(\theta)$. The evaluation of the potential energy matrix in the direct product DVR basis becomes trivial due to the localized nature of the basis states, $\langle \tilde{\psi}_{R,i}\tilde{\phi}_{\theta,m}|V(R,\theta)|\tilde{\psi}_{R,j}\tilde{\phi}_{\theta,n}\rangle \approx V(R_i,\theta_m)\delta_{i,j}\delta_{m,n}$. We estimate the error associated with this approximate representation of the potential energy matrix to be no more than a few percent. A discussion of the error associated with various discrete variable representations can be found in [11]. Once the potential energy matrix is obtained it is transformed to the $\psi_{R,n}(R) \times \phi_{\theta,n}(\theta)$ basis using an unitary matrix $\boldsymbol{T} = \boldsymbol{T_R} \times \boldsymbol{T_\theta}$ and added to the kinetic energy matrix [12]. This gives us the full Hamiltonian matrix in the $\psi_{R,n}(R) \times \phi_{\theta,n}(\theta)$ basis, which can then be diagonalized to yield the energy eigenstates.

IV. BOUND STATES

We find 357 odd eigenstates and 365 even eigenstates with energies below the classical dissociation energy. In this section we relate the structure of these eigenstates to the classical POs that exist at similar energies. The classical vibrational dynamics is governed by a series of saddle-center and period doubling bifurcations that occur as the energy is increased [5]. The new POs that are born from these bifurcations give rise to new structures in the quantum eigenstates.

At low energies the system is largely integrable and the eigenstates can be assigned approximate quantum numbers n_R and n_B, representing the number of nodes the eigenstate has along the "stretching" normal mode PO [R] and the "bending" normal mode PO [B]. At low energies HOCl has an approximate Fermi resonance between bending and stretching motions making $n_B \approx 2n_R$. The low-energy eigenstates can thus be arranged into polyads, groups of states that share the same polyad number $P = n_R + 2n_B$ and thus have similar energies. Figure 2 shows the five eigenstates belonging to the $P = 8$ polyad. The lowest energy eigenstate in the polyad has $P/2$ nodes arranged along PO [B]. Each higher energy eigenstate in the polyad removes one node along [B] and replaces it with two nodes along [R], with the most energetic eigenstate having all P nodes arranged along PO [R]. Eigenstates in other polyads continue to follow this simple evolution of nodes along [B] and [R]. However, for energies above $E = 10,000$ cm^{-1}, the Fermi resonance causes PO [R] to take on an increasingly curved shape. As a result, eigenstates that are aligned along [R] also exhibit a pronounced curvature as is evident in Fig. 3(a).

Just below $E = 13,900$ cm^{-1} the classical system undergoes its first bifurcation, a saddle-center bifurcation giving birth to a new PO [D] that replaces [R] as the PO that stretches along the dissociation channel. Classically, this bifurcation occurs at a specific energy giving birth to a fully formed PO [D]. The quantum manifestation of this bifurcation is more gradual and does not occur at one specific energy. Figures 3(b) and 3(c) show two eigenstates whose structures are strongly influenced by PO [D]. The eigenstate in Fig. 3(b) has an energy
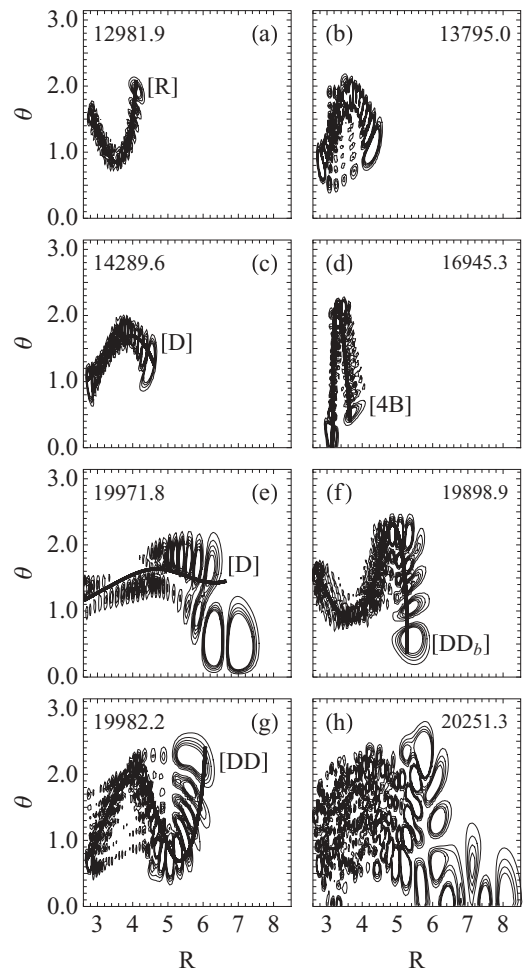

FIG. 3. Energy eigenstates (below dissociation) together with their corresponding periodic orbits (POs) at the same energy. The eigenstate in (b) resembles PO [D] but the PO does not exist at this energy. The eigenstate in (h) is an example of a "chaotic" eigenstate that does not have a corresponding PO. The energy of each state (in cm^{-1}) is indicated at the top. Coordinate R is measured in units of a_0.

below the classical bifurcation energy, and while its probability is not as cleanly aligned as the eigenstate in Fig. 3(c), it is clearly being influenced by the soon-to-be-born PO [D].

Continuing to higher energies, PO [B] undergoes a period doubling giving birth to PO [2B], which then period doubles into PO [4B]. The classical PO [4B] becomes unstable very quickly as the energy is increased. However, the unstable PO [4B] continues to scar eight of the even eigenstates, one of which is shown in Fig. 3(d). We find no odd eigenstates that take their structure from PO [4B]. The eight even eigenstates that are scarred by [4B] are the reason for the differing numbers of even and odd bound states.

As the energy approaches the dissociation energy, PO [D] becomes unstable. However, it continues to scar those eigenstates that stretch farthest along the dissociation channel. Figure 3(e) shows an eigenstate scarred by the now unstable PO [D]. The eigenstate extends farther in R than [D] does and curves down to lower θ values. The eigenstate crosses over a slight hill in the potential energy near $(R,\theta) = (6.33a_0,0.35)$
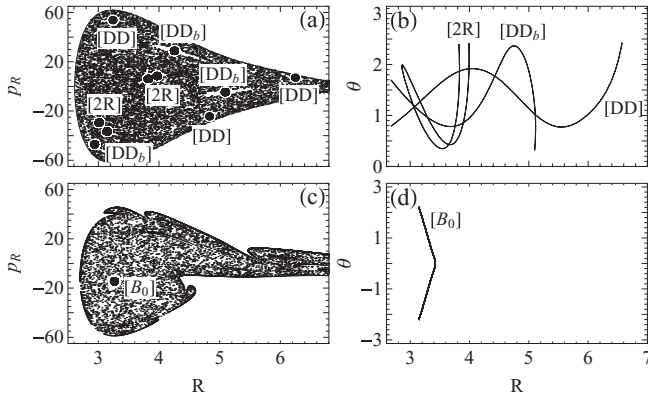
FIG. 4. (a) Poincaré surface of section for $E = 20,150$ cm^{-1} (just below dissociation). (b) Stable periodic orbits (POs) for $E = 20,150$ cm^{-1}. (c) Poincaré surface of section for $E = 21,000$ cm^{-1} (just above dissociation). (d) Stable PO for $E = 21,000$ cm^{-1}. Coordinates R and p_R are measured in units of a_0 and $\hbar/a_0$, respectively.

to smaller θ values where the potential energy is lower. The eigenstate is not localized along a single curve the way [D] is and is thus influenced by the region of lower potential energy near $\theta = 0$. There are also two new types of eigenstates that come into existence in this energy regime. These eigenstates, shown in Figs. 3(f) and 3(g), take their structure from the classical POs [DD] and [DD$_b$] which are born out of saddle-center bifurcations near $E = 20,000$ cm^{-1}. Classically [DD] represents the new "dissociation" PO at these energies. However, because PO [D] continues to scar eigenstates after going unstable, PO [DD] plays a much smaller role in the quantum dissociation process.

The classical dynamics becomes increasingly chaotic as the energy approaches the dissociation energy. The Poincaré surface of section in Fig. 4(a) shows the classical phase space almost completely engulfed by chaos at $E = 20,150$ cm^{-1}. The quantum system shows some evidence of this chaos. Of the approximately 360 even or odd bound states, we find 5 or 6 eigenstates that are spread over a large region of configuration space with no discernible nodal structure. Figure 3(h) shows one of these "chaotic" eigenstates. HOCl does possess several eigenstates with somewhat messy nodal structures. However, these states are fairly well localized in R and θ and can be associated with various classical POs. The high degree of regularity in the quantum domain is consistent with the fact that an integrable Fermi resonance Hamiltonian has been used to successfully reproduce the quantum spectrum all the way up to 98% of the dissociation energy [13]. The subject of classical chaos versus quantum regularity for vibrational eigenstates in HOCl has been discussed in [6].

V. REACTION MATRIX THEORY

The HO-Cl quasibound states are calculated using the reaction matrix theory of Wigner and Eisenbud [14,15]. Reaction matrix theory, for the case of 2D polar coordinates, is worked out in detail in [16]. Here we outline the application of reaction matrix theory to our 2D model of HOCl following the same notation as used in [16].

We start by partitioning configuration space into an asymptotic region where the effect of the potential energy is negligible and a reaction region where the potential energy must be taken into consideration. For HOCl the potential energy is essentially flat beyond $R = 8a_0$ so we choose the boundary of the reaction region to be at $R_{\max} = 10a_0$. The dynamics in the reaction region is described by a set of orthonormal basis states $\xi_j(R,\theta)$ that satisfy the zero-slope boundary condition $\frac{\partial \xi_j}{\partial R}|_{R_{\max}} = 0$. The basis states are eigenvectors of the HOCl Hamiltonian which, due to the boundary condition at $R = R_{\max}$, have discrete eigenvalues λ_j.

The reaction region eigenstates are calculated using DVR as described in Sec. III. To satisfy the zero-slope boundary condition we use $R_{\min} = 0$ and a primitive basis for R consisting of 250 Bessel functions, $\phi_{R,n}(R) = C_{1,n} J_1(\alpha_{1,n} R/R_{\max})$, where $\alpha_{1,n}$ is the nth zero of $\frac{dJ_1}{dR}$ and $C_{1,n}$ is the normalization constant. The reaction-region eigenstates can be written as $\xi_j(R,\theta) = \sum_{m=1}^{60} \xi_{j,m}(R)\phi_{\theta,m}(\theta)$, where $\phi_{\theta,m}(\theta)$ is defined in Sec. III and $\xi_{j,m}(R) = \sum_{n=1}^{130} a_{j,m,n}\psi_{R,n}(R)$. $\psi_{R,n}(R)$ is the nth eigenstate of the 1D eigenproblem obtained by setting $\theta = \theta_{eq}$ in the Hamiltonian and the coefficients $a_{j,m,n}$ come from solving the 2D eigenproblem in the reaction region.

The scattering eigenstate, in the reaction region, can be expanded in terms of the reaction-region basis states as

$$\Psi_E(R \leqslant R_{\max},\theta) = \sum_{j=1}^{N} \gamma_j(E)\xi_j(R,\theta), \qquad (5)$$

where $N = 60 \times 130$ is the total number of basis states used in the reaction region. Coupling the reaction region to the asymptotic region and requiring the scattering eigenstate to be continuous at $R = R_{\max}$ leads to the following equation for $\gamma_j(E)$:

$$\gamma_j(E) = \frac{\hbar^2 R_{\max}}{2\mu_1(\lambda_j - E)} \sum_{m=1}^{60} \xi_{j,m}^*(R_{\max})\frac{\partial \Phi_m(k_m R)}{\partial R}\bigg|_{R_{\max}}. \qquad (6)$$

In the asymptotic region the potential energy is taken to be constant and equal to the dissociation energy $D_e = 20,312.3$ cm^{-1}. The scattering eigenstate, in the asymptotic region, can be written in terms of incoming and outgoing cylindrical waves as

$$\Psi_E(R \geqslant R_{\max},\theta) = \sum_m \Phi_m(k_m R)\phi_{\theta,m}(\theta)$$

$$= \sum_{m=1}^{60} \left[A_m H_m^{(2)}(k_m R) + B_m H_m^{(1)}(k_m R)\right]$$

$$\times \phi_{\theta,m}(\theta), \qquad (7)$$

where $H_m^{(1,2)}$ are Hankel functions and $k_m = \sqrt{2\mu_1(E - D_e)/\hbar^2 - m^2\mu_1/\mu_2 r_0^2}$. We set the incoming amplitudes A_m equal to 0 for $m > M$, where M is the first angular momentum value for which k_m is imaginary, and equal to 1 otherwise. The amplitudes of the incoming partial waves A_m are related to the amplitudes of the outgoing partial waves B_m by the scattering matrix **S** so that $\mathbf{B} = \mathbf{S} \cdot \mathbf{A}$, where **B(A)** is a

column matrix containing amplitudes $B_m(A_m)$. The scattering matrix can be written as

$$\mathbf{S} = -\mathbf{H}^{(2)} \cdot \{\mathbf{1}_M + 2i\,R_{\max}\mathbf{v}^\dagger \cdot [\mathbf{H}^{\text{eff}}(E) - E\mathbf{1}_N]^{-1} \cdot \mathbf{x}\} \cdot \mathbf{H}^{(1)}. \tag{8}$$

Here $\mathbf{H}^{(1,2)}$ are $M \times M$ diagonal matrices with elements $H_m^{(1,2)}(k_m R_{\max})$, $\mathbf{1}_M$ is the $M \times M$ identity matrix, $\mathbf{v}^\dagger = (\mathbf{H}^{(1)}\mathbf{H}^{(2)})^{-1} \cdot \mathbf{w}^\dagger$, and $\mathbf{x} = \mathbf{w} \cdot \boldsymbol{\beta}$. The matrix $\mathbf{w}$ has elements $\mathbf{w}_{j,m} = \sqrt{\frac{\hbar^2}{2\mu_1}}\xi_{j,m}^*(R_{\max})$ and $\boldsymbol{\beta}$ is the imaginary part of $\dot{\mathbf{H}}^{(1)}\mathbf{H}^{(2)}$. We have written the scattering matrix in terms of a non-Hermitian effective Hamiltonian given by

$$\mathbf{H}^{\text{eff}}(E) = \mathbf{H}_{\text{in}} - R_{\max}\mathbf{w} \cdot \dot{\mathbf{H}}^{(1)} \cdot (\mathbf{H}^{(2)})^{-1} \cdot \mathbf{w}^\dagger, \tag{9}$$

where $\mathbf{H}_{\text{in}}$ is an $N \times N$ diagonal matrix of reaction-region eigenvalues λ_j. From Eq. (8) it is clear that the poles of the scattering matrix occur at complex energies corresponding to the eigenvalues of the effective Hamiltonian. These complex energy poles correspond to quasibound states of the system.

The (m,m')th element of the scattering matrix couples the m'th incoming partial wave to the mth outgoing partial wave. The magnitude of $\mathbf{S}_{m,m'}$ is a measure of how strongly the mth and m'th partial waves interact during the scattering process. Figure 5 shows the magnitudes $|\mathbf{S}_{1,1}|$, $|\mathbf{S}_{1,2}|$, and $|\mathbf{S}_{1,3}|$ as a function of energy. The peaks and dips in Fig. 5 represent energies for which the partial waves are significantly affected by the scattering process. Peaks and dips in $|\mathbf{S}_{m,m'}|$ thus correspond to quasibound states with the width of the peak being inversely related to the lifetime of the quasibound state.
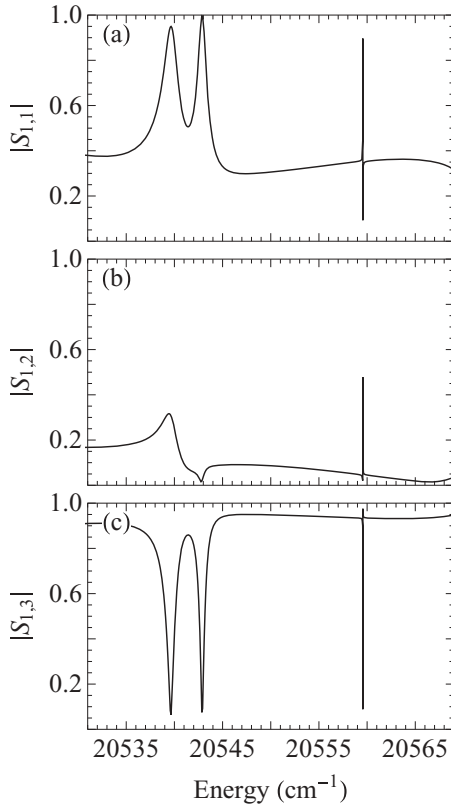

FIG. 5. Magnitudes of scattering matrix elements (a) $|\mathbf{S}_{1,1}|$, (b) $|\mathbf{S}_{1,2}|$, and (c) $|\mathbf{S}_{1,3}|$.

Each peak in Fig. 5 is centered around an energy matching the real part of an eigenvalue of the effective Hamiltonian.

VI. QUASIBOUND STATES

The complex-energy eigenvalues of the effective Hamiltonian, $\mathcal{E}_n = \mathcal{E}_{n,0} - i\Gamma_n/2$, where $\mathcal{E}_{n,0}$ and Γ_n are real, represent quasibound states with lifetimes $\tau_n = \hbar/\Gamma_n$. For HOCl we find quasibound states with lifetimes that range over 5 orders of magnitude, from 10^{-12} to 10^{-7} s. In this section we connect quasibound states with various lifetimes to the structures in the underlying classical phase space that support them.

To relate quasibound states to structures in the classical phase space, we construct Husimi distributions for the scattering energy eigenstates, $\Psi_E(R,\theta)$, evaluated at the real part $E = \mathcal{E}_{n,0}$ of the quasibound state energies. A Husimi distribution acts as a quantum mechanical analog to a classical Poincaré surface of section showing how the quantum state's probability is distributed in phase space [17]. Lu and Kellman have shown Husimi distributions to be very useful for organizing sequences of bound energy eigenstates and assigning approximate quantum numbers to eigenstates when the classical dynamics is a mixture of regular and chaotic motion [18]. Here we apply Husimi distributions to a system in which the classical dynamics is almost entirely chaotic.

There exists some freedom in how one defines a Husimi distribution. We follow the definition used in [6] where the Husimi distribution ρ for a scattering energy eigenstate $\Psi_E(R,\theta)$ is given by

$$\rho(\mathbf{q}',\mathbf{p}') = |\langle \Phi_{\mathbf{q}',\mathbf{p}'}, \Psi_E \rangle|^2, \tag{10}$$

where $\Phi_{\mathbf{q}',\mathbf{p}'}$ is the product of 1D minimum uncertainty wave packets

$$\Phi^{1D}(R',p_R') = \frac{1}{[2\pi(\Delta R)^2]^{1/4}}\exp\left[-\frac{1}{4(\Delta R)^2}(R'-R)^2 \right.$$
$$\left. + \frac{i}{\hbar}p_R'(R'-R)\right] \tag{11}$$

and

$$\Phi^{1D}(\theta',p_\theta') = \frac{1}{[2\pi(\Delta\theta)^2]^{1/4}}\exp\left[-\frac{1}{4(\Delta\theta)^2}(\theta'-\theta)^2 \right.$$
$$\left. + \frac{i}{\hbar}p_\theta'(\theta'-\theta)\right]. \tag{12}$$

The half-widths of the wave packets are determined from the classical Hamiltonian by $\Delta q_i = \sqrt{\frac{\hbar}{2}}(\frac{\partial^2 T}{\partial p_i^2})^{1/4}(\frac{\partial^2 V}{\partial q_i^2})^{-1/4}$ evaluated at the equilibrium coordinates. To project the Husimi distribution onto the $\theta = \theta_{\text{eq}}$ plane $|\langle \Phi_{\mathbf{q}',\mathbf{p}'}, \Psi_E \rangle|^2$ is integrated over R and θ, θ' is set equal to θ_{eq}, and p_θ' is determined by requiring the classical energy to be equal to the real part of the quasibound-state energy.

Figure 6(a) shows the state $\Psi_E(R,\theta)$ at the energy of the longest-lived quasibound state, $E = \mathcal{E}_0 = 20,374.94\,\text{cm}^{-1}$ with $\Gamma = 3.15 \times 10^{-5}\,\text{cm}^{-1}$ [we call states $\Psi_E(R,\theta)$ quasibound states when they have energies $E = \mathcal{E}_0$ corresponding to the real part of the complex energies of the effective
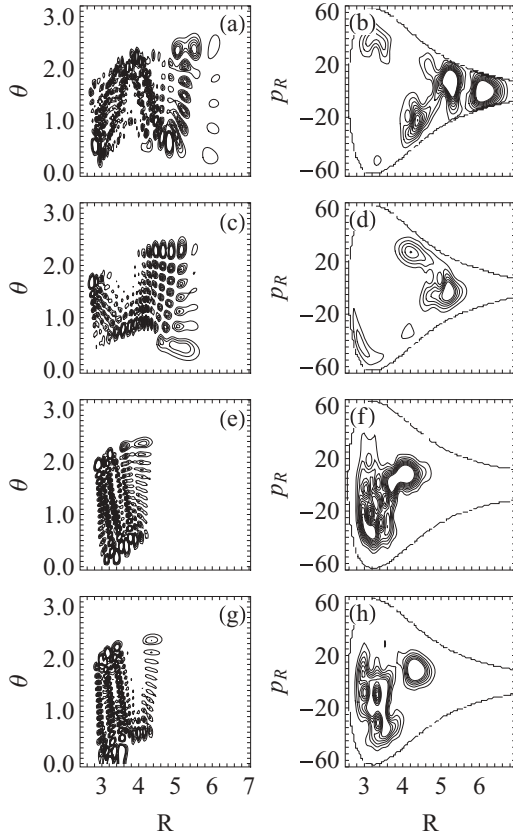
FIG. 6. Plots of scattering energy eigenstates $|\Psi_E(R,\theta)|^2$, and their Husimi plots, at energies $E = \mathcal{E}_0$, the real part of a complex eigenenergy of the effective Hamiltonian. (a, b) $\mathcal{E} = 20{,}374.94 - i1.58 \times 10^{-5}$ cm^{-1}; (c, d) $\mathcal{E} = 20{,}343.17 - i8.48 \times 10^{-5}$ cm^{-1}; (e, f) $\mathcal{E} = 20{,}782.74 - i3.36 \times 10^{-4}$ cm^{-1}; (g, h) $\mathcal{E} = 20{,}515.10 - i6.84 \times 10^{-4}$ cm^{-1}. These states are fairly long-lived. Coordinates R and p_R are measured in units of a_0 and $\hbar/a_0$, respectively.
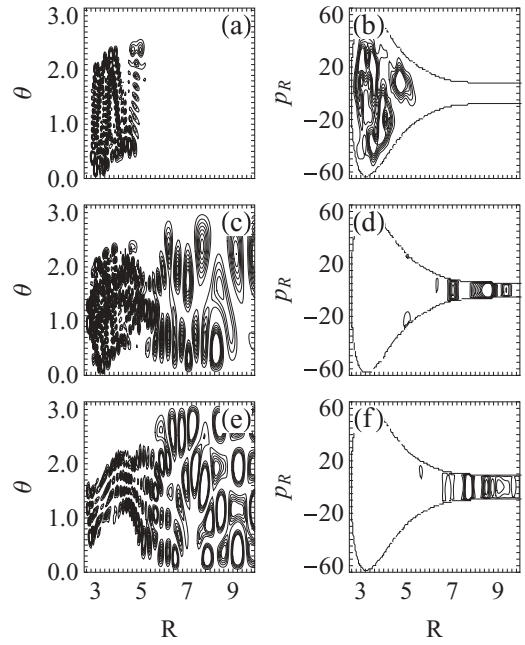

FIG. 7. Plots of scattering energy eigenstates $|\Psi_E(R,\theta)|^2$, and their Husimi plots, at energies $E = \mathcal{E}_0$, for short-lived quasibound states. (a, b) $\mathcal{E} = 20{,}559.56 - i1.24 \times 10^{-3}$ cm^{-1}; (c, d) $\mathcal{E} = 20{,}433.76 - i0.03$ cm^{-1}; (e, f) $\mathcal{E} = 20{,}682.37 - i2.00$ cm^{-1}. Coordinates R and p_R are measured in units of a_0 and $\hbar/a_0$, respectively.

Hamiltonian]. The quasibound state's probability is greatest along a curve resembling the classical PO [DD] shown in Fig. 4(b). Comparing the Husimi distribution in Fig. 6(b) to the classical surface of section in Fig. 4(a), we see that this quasibound state is supported mainly by PO [DD]. However, there is also a region of high probability near PO [DD$_b$] in phase space. The additional influence of [DD$_b$] is likely the reason for the somewhat messy nodal pattern in Fig. 6(a) as well as the reason that the quasibound state is more compressed in R than PO [DD]. The POs in Figs. 4(a) and 4(b) are unstable for energies above the dissociation energy, however, they continue to influence the quasibound states.

Slightly shorter-lived quasibound states are also strongly influenced by various unstable POs in the classical dynamics. The quasibound states in Figs. 6(c) and 6(e) correspond to complex eigenvalues of the effective Hamiltonian given by $\mathcal{E} = 20{,}343.17 - i8.48 \times 10^{-5}$ cm^{-1} and $\mathcal{E} = 20{,}782.74 - i3.36 \times 10^{-4}$ cm^{-1} and are supported by POs [DD$_b$] and [2R], respectively. The quasibound state in Fig. 6(g) with $\mathcal{E} = 20{,}515.10 - i6.84 \times 10^{-4}$ cm^{-1} is the longest-lived quasibound state with even parity. This quasibound state is partially supported by POs [B$_0$] and [2R], however, its probability is

spread over a wider region of phase space than is seen in the longer-lived quasibound states.

Short-lived quasibound states display messier nodal structures and probabilities that begin to stretch into the asymptotic region. Figure 7(a) shows a quasibound state with $\mathcal{E} = 20{,}559.56 - i1.24 \times 10^{-3}$ cm^{-1}. This state has a messy nodal structure and probability spread throughout the majority of phase space. This quasibound state is influenced by the overall chaotic nature of the classical phase space with a nodal pattern and Husimi distribution that does not match any of the classical POs. The quasibound states with the shortest lifetimes have nodes that lie primarily along the dissociation channel and Husimi distributions that are concentrated at very large R values. Figures 7(c) and 7(e) show two such states, with $\mathcal{E} = 20{,}433.76 - i0.03$ cm^{-1} and $\mathcal{E} = 20{,}682.37 - i2.00$ cm^{-1}, respectively.

VII. WIGNER-SMITH DELAY TIME

The effective Hamiltonian in Eq. (9) provides a convenient way of obtaining the Wigner-Smith delay time. The delay time is a measure of the amount of time a particle incident with energy E is delayed in the reaction region relative to free motion. The Wigner-Smith delay time can be written in terms of the eigenvalues of the effective Hamiltonian as [16]

$$\tau_{WS} = -i\hbar \left[\sum_{m=1}^{M} \frac{H_m^{(1)}(k_m R_{\max})}{H_m^{(2)}(k_m R_{\max})} \frac{d}{dE}\left(\frac{H_m^{(2)}(k_m R_{\max})}{H_m^{(1)}(k_m R_{\max})} \right) \right.$$
$$\left. - \sum_{n=1}^{N} \frac{2i\,\Gamma_n/2}{(E - \mathcal{E}_{n,0})^2 + (\Gamma_n/2)^2} \right]. \tag{13}$$
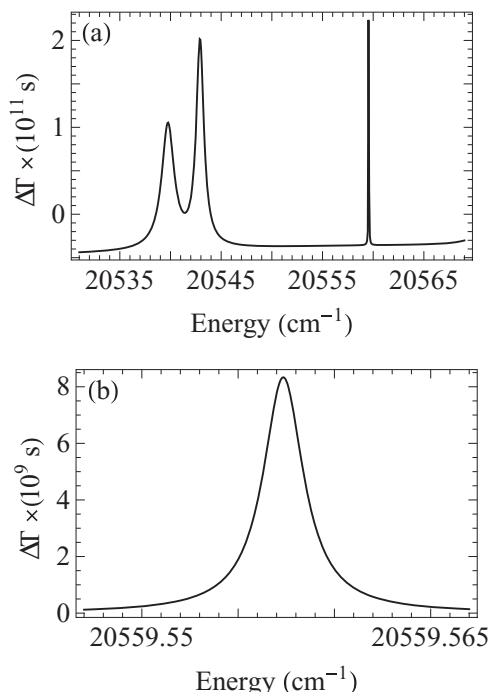
FIG. 8. (a) Wigner-Smith delay time showing peaks corresponding to quasibound states. (b) Enlargement of the very thin peak in (a).

Figure 8(a) shows the Wigner-Smith delay time for a range of energy containing three peaks. The very thin peak near $E_1 = 20{,}560$ cm^{-1} represents a long-lived quasibound state, with the broader peaks representing much shorter-lived quasibound states. Figure 8(b) shows an enlargement of the very thin peak. The peak occurs at the same energy as predicted by the real part of the eigenvalue of the effective Hamiltonian. The peak has a maximum of $\delta T = 8.55 \times 10^{-9}$ s and a full-width at half-maximum of $\delta E = 0.0024$ cm^{-1}. The delay time can be related to the lifetime of the quasibound state through $\delta T = \hbar/4\Gamma$ and $\delta E = \Gamma$ [19]. The value of Γ obtained from the delay time agrees very well with the value obtained directly from the eigenvalue of the effective Hamiltonian.

VIII. SUMMARY

We have used a potential-optimized DVR to calculate the bound vibrational states of a 2D model of HOCl. The structures of the vibrational eigenstates correspond closely to the classical POs studied in [5]. A number of new types of eigenstates appear at energies close to the bifurcation energies in the classical system. While the classical system exhibits a high degree of chaos at energies near the dissociation energy, the quantum system remains predominantly ordered all the way up to the HO + Cl dissociation energy.

Using the reaction matrix theory of Wigner and Eisenbud together with a potential-optimized DVR, we have calculated the HO-Cl quasibound states with energies slightly above the dissociation energy. The lifetimes of these quasibound states range over 5 orders of magnitude. By examining the structure of quasibound states in configuration space and in Husimi distributions, we find that many of the quasibound states are supported by unstable POs in the classical system. The lifetime of the quasibound state is loosely correlated with the amount of motion along coordinate θ exhibited by the classical PO that supports it.

The results presented here contribute to the growing body of work on quantum-classical correspondence and semiclassical methods in systems whose classical dynamics exhibit varying degrees of chaos. It has been known that unstable POs can support quantum eigenstates since Heller's seminal work on PO scars [20]. More recently there have been several successful efforts to construct accurate semiclassical wave functions based on the classical dynamics using POs, heteroclinic orbits, and invariant tori and cantori [21–24]. These studies have all focused on bound systems with mixed classical phase spaces. The significant role played by unstable POs in supporting long-lived quasibound states in HOCl suggests that these methods may continue to be valuable tools for studying unbound systems.

[1] J. Hauschildt, J. Weiß, C. Beck, S. Yu. Grebenshchikov, R. Düren, R. Schinke, and J. Koput, Chem. Phys. Lett. **300**, 569 (1999).

[2] S. Skokov and J. Bowman, J. Chem. Phys. **111**, 4933 (1999).

[3] J. Weiß, J. Hauschildt, S. Yu. Grebenshchikov, R. Düren, R. Schinke, J. Koput, s. Stamatiadis, and S. C. Farantos, J. Chem. Phys. **112**, 77 (2000).

[4] H. Y. Mussa and J. Tennyson, Chem. Phys. Lett. **366**, 449 (2002).

[5] A. M. Barr, K. Na, L. E. Reichl, and C. Jung, Phys. Rev. E **79**, 026215 (2009).

[6] M. Joyeux, D. Sugny, M. Lombardi, R. Jost, R. Schinke, S. Skokov, and J. Bowman, J. Chem. Phys. **113**, 9610 (2000).

[7] M. Joyeux, S. C. Farantos, and R. Schinke, J. Phys. Chem. A **106**, 5407 (2002).

[8] H. Lee, C. Jung, and L. E. Reichl, Phys. Rev. B **73**, 195315 (2006).

[9] K. Na, D. Jarukanont, and L. E. Reichl, Phys. Rev. E **77**, 046208 (2008).

[10] J. Echave and C. Clary, Chem. Phys. Lett. **190**, 225 (1992).

[11] J. C. Light, I. P. Hamilton, and J. V. Lill, J. Chem. Phys. **82**, 1400 (1985).

[12] W. Schweizer, *Numerical Quantum Dynamics, Progress in Theoretical Chemistry and Physics 9* (Kluwer Academic, Norwell, MA, 2001).

[13] R. Jost, M. Joyeux, S. Skokov, and J. Bowman, J. Chem. Phys. **111**, 6807 (1999).

[14] E. P. Wigner and L. E. Eisenbud, Phys. Rev. **72**, 29 (1949).

[15] A. M. Lane and R. G. Thomas, Rev. Mod. Phys. **30**, 257 (1958).

[16] A. M. Barr and L. E. Reichl, Phys. Rev. A **81**, 022707 (2010).

[17] L. E. Reichl, *The Transition to Chaos*, 2nd ed. (Springer-Verlag, New York, 2004).

[18] Z.-M. Lu and M. E. Kellman, Chem. Phys. Lett. **247**, 195 (1995).

[19] A. Bohm, *Quantum Mechanics: Foundations and Applications*, 3rd ed. (Springer-Verlag, New York, 2001).

[20] E. J. Heller, Phys. Rev. Lett. **53**, 1515 (1984).

[21] S. Yang and M. E. Kellman, Phys. Rev. A **66**, 052113 (2002).

[22] S. Tomsovic and E. J. Heller, Phys. Rev. Lett. **70**, 1405 (1993).

[23] S. Yang and M. E. Kellman, Phys. Rev. A **62**, 022105 (2000).

[24] S. Yang and M. E. Kellman, Chem. Phys. **322**, 30 (2006).